

Understanding and Optimizing Capacitance Performance in Reduced Graphene-Oxide Based Supercapacitors

Srinivas Gadipelli,* Jian Guo, Zhuangnan Li, Christopher A. Howard, Yini Liang, Hong Zhang, Paul R. Shearing, and Dan J. L. Brett*

Reduced graphene-oxide (RGO)-based electrodes in supercapacitors deliver high energy/power capacities compared to typical nanoporous carbon materials. However, extensive critical analysis of literature reveals enormous discrepancies (up to 250 F g^{-1}) in the reported capacitance (variation of $100\text{--}350 \text{ F g}^{-1}$) of RGO materials synthesized under seemingly similar methods, inhibiting an understanding of capacitance variation. Here, the key factors that control the capacitance performance of RGO electrodes are demonstrated by analyzing and optimizing various types of commonly applied electrode fabrication methods. Beyond usual data acquisition parameters and oxidation/reduction properties of RGO, a substantial difference of more than 100% in capacitance values (with change from 190 ± 20 to $340 \pm 10 \text{ F g}^{-1}$) is found depending on the electrode preparation method. For this demonstration, ≈ 40 RGO-based electrodes are fabricated from numerous distinctly different RGO materials via typically applied methods of solution (aqueous and organic) casting and compressed powders. The influence of data acquisition conditions and capacitance estimation practices are also discussed. Furthermore, by optimizing electrode processing method, a direct surface area governed capacitance relationship for RGO structures is revealed.

1. Introduction

Supercapacitors (SCs) designed with nanoporous carbon materials (NPCs) have shown to deliver unprecedented energy and power densities. The relatively low-cost and high tunability of these NPCs makes them an attractive proposition for a wide range of applications.^[1–4] Meanwhile, SCs are being increasingly integrated with battery and fuel cell systems to enhance efficiencies and overall capabilities of electrochemical energy storage systems (EESs).^[5–7] The energy storage mechanism of NPCs-based SCs is predominantly via the electrical double layer capacitance (EDLC). In this mechanism, upon charging, electric charges and adsorbed counter ions accumulate on the electrode surface and it is this phenomenon that directly defines the output capacitance or energy/power density. Such adsorption is strongly governed by the surface binding energy and


accessible surface related parameters; surface heterogeneity, pore-size, pore volume, and specific surface area (SSA). In addition, electrochemical activity is promoted by charge/electron transfer dynamics/phenomena and electrolyte–electrode interfacial area. Given these interlinked and widely tunable parameters, numerous synthesis routes have been explored, aiming to produce high performing NPC based nanostructured electrodes.^[8] Impressive capacitance performance, including high gravimetric energy and power densities has been achieved with highly porous NPC materials that are usually produced via template or metal salt impregnation followed by high temperature chemical activation or pyrolysis.^[9–11] However, the potential of these systems (e.g., cost per unit power delivery along with volumetric densities and solid-state devices) is compromised due to poorly controlled porosity, modest electrical conductivity, and density of the key structural features required for charge storage.^[9,11–14] The optimal characteristics often have complex trade-off relationships. For example, optimizing for ultrahigh porosity in NPCs to improving the ion/charge adsorption capacity can also result in detrimental overall performance (e.g., rate capability, areal capacitance, and charge accumulation density, which is high in ion size matching pore widths but reduced in larger pore widths) because highly porous materials also often have a high large pore size fraction.^[9,12] High porosities in NPCs can

S. Gadipelli, J. Guo, Y. Liang, H. Zhang
College of Physics
Sichuan University
Chengdu 610064, China
E-mail: s.gadipelli@ucl.ac.uk; s.gadipelli@scu.edu.cn

S. Gadipelli, P. R. Shearing, D. J. L. Brett
Electrochemical Innovation Lab
Department of Chemical Engineering
University College London
London WC1E 7JE, UK
E-mail: d.brett@ucl.ac.uk

Z. Li
Department of Materials Science and Metallurgy
University of Cambridge
Cambridge CB3 0FS, UK

C. A. Howard
Department of Physics & Astronomy
University College London
London WC1E 6BT, UK

 The ORCID identification number(s) for the author(s) of this article can be found under <https://doi.org/10.1002/smtd.202201557>

© 2023 The Authors. Small Methods published by Wiley-VCH GmbH. This is an open access article under the terms of the Creative Commons Attribution License, which permits use, distribution and reproduction in any medium, provided the original work is properly cited.

DOI: 10.1002/smtd.202201557

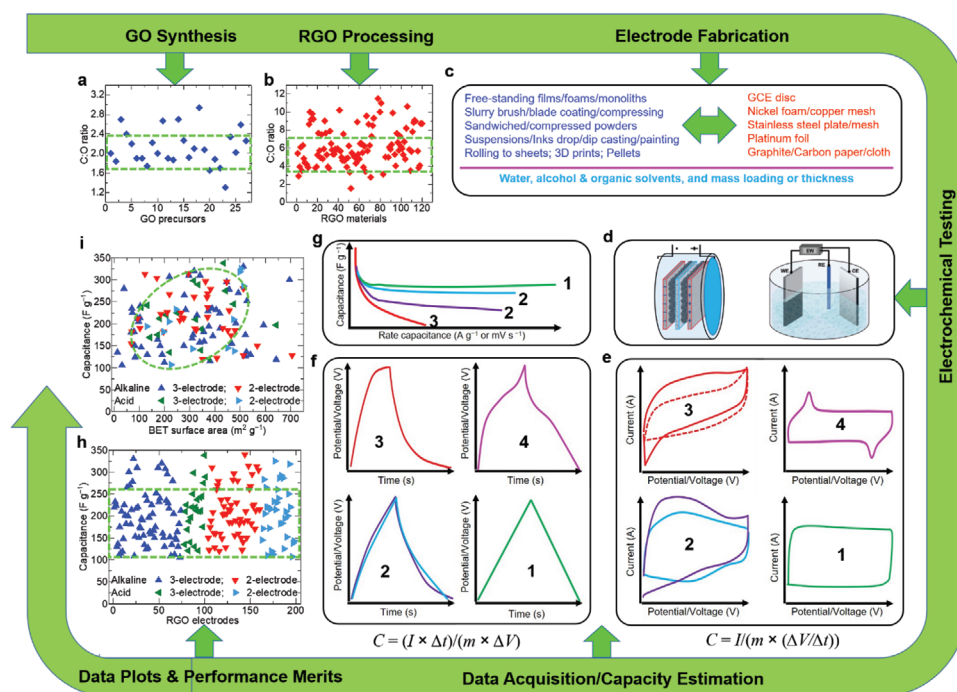


Figure 1. Summary overview of literature on RGO based supercapacitors performance with materials synthesis and electrode fabrication methods, electrochemical measurements, and charge storage characteristics. a) C:O ratio of different GO precursors. b) C:O ratio of RGO materials. c) Electrode fabrication routes. d) Electrochemical test systems. e,f,g) Typically observed CV, GCD, and rate capacitance curves: green curves (in plot 1) are mostly associated with ideal EDLC or with highly graphitized NPCs; light blue and dark purple curves (in plot 2) represent combined surface related EDLC and pseudocapacitive related Faradic redox reactions, and purple curves in (plot 4) are associated with Faradic redox reactions. The red curves (in plot 3) are associated with experimental condition with extended potential range and/or ultra-low current densities. h) Specific capacitance values of ≈ 200 RGO samples taken from the literature (where possible data is deduced from GCD discharge curves at $0.5\text{--}1.0\text{ A g}^{-1}$ or CV curves). i) Specific surface area dependence of specific capacitance values (taken from same condition as in (h); see Table S1, Supporting Information for more details for GO, RGO samples, along with C:O ratio, measurement conditions, electrolyte, capacitance values, and references). To be more realistic, capacities are deduced at very low current densities or from unrealistic CV and GCD curves and structures with significant contribution from Faradic redox reactions (e.g., the red and purple data, respectively in (e,f) has been omitted where possible as these conditions tend to overestimate capacity). For comparison, RGO structures generated under high temperature (of more than $300\text{ }^{\circ}\text{C}$ or $400\text{ }^{\circ}\text{C}$) reduction, activation, pyrolysis, and carbonization routes are excluded from this figure and table data.

also increase defect/ sp^3 carbon concentration at the expense of their electrically-conductive sp^2 graphite components and furthermore, highly porous materials can have low densities. These factors can combine to increase the resistive path for electron transport; thus, limiting the performance. Furthermore, 3D NPC particles with typical sizes ranging from hundreds of nanometers to microns show considerable variation in their energy storage capacity;^[10,11,15] large carbon particles can limit overall electrochemical activity due to increased resistive electron path length. For example, porous carbons synthesized via the uniform pore structure metal-organic frameworks (MOFs) and their subfamily zeolitic imidazolate frameworks (ZIFs) as sacrificial templates have shown a considerable variation in their capacitance values and rate performance.^[11,15-19] Carbons produced from biomass or inorganic or polymeric precursors require high temperatures treatment to improve their graphitization; and thus, electrical conductivity.^[9-11,15-19]

Highly conducting 2D layered structures, such as graphite, graphitic carbon nitride, and metal carbides (MXenes)/dichalcogenides, are promising candidate materials for SC electrodes if their layers are manipulated to accommodate charge storage.^[20-25] The most common method is to

delaminate the layers fully in liquids and reassemble them to form a suitable nanostructured macroscopic material.^[12,13,26] Most typical graphene-based materials are scalably derived from bulk graphite, via oxidation, to form graphite-oxide or graphene-oxide (GO) for processing/delamination, and then chemically and/or thermally reduced to form conductive structures (RGO). This area of research is extremely active and many different approaches have generated a huge range of conducting graphene networks with exceptionally varied porosity from ultra-small/slit-like pores to micro-porosity and high in meso- and macro-porosity that can potentially host high charge storage and ion transfer to form extensive electrical double-layers.^[9-14,21-25,27-42] Thus, RGO-based graphene networks are demonstrating attractive energy storage capacities in SCs. However, progress is held back by a lack of understanding of how to optimize these structures (and how they are processed) for the most efficient performances. Evidence of trends of structure-related capacity in the RGO samples is currently lacking. As summarized in **Figure 1**; Table S1, Supporting Information, an analysis of more than 200 RGO samples reveals a large variation in capacitance values when measured under aqueous (acid and alkaline) electrolyte. The actual experimental parameters, such

as whether the measurement is performed in two- or three-electrode configuration, in acidic or alkaline electrolyte, and at which current density or scan rate the capacitance is deduced, are all detailed in Figure 1h; Table S1, Supporting Information. Here, the associated oxidation/reduction levels in GO/RGO materials and SSA relevant capacitance are presented in Figures 1a,b and 1i, respectively. The typical cyclic voltammetry (CV) and galvanostatic charge–discharge (GCD) curves for capacity calculation are shown in Figure 1e,f.^[43] The data shows a large variation in capacitance values between 100 and 350 F g⁻¹ for the RGO electrode materials produced under similar reduction routes at mild temperatures of ≈300 °C or lower; this includes solution and solid-state reduction routes. The second noteworthy observation is that the data in Figure 1h or 1i show no conclusive evidence that redox reactions of acidic electrolyte yield favorable capacitance values compared to alkaline electrolyte. In fact, the capacitance is unpredictable in both electrolytes and varies over a similar range. The third notable point is that capacitance values of three-electrode and two-electrode measurement systems show large discrepancies and span between 100 and 350 F g⁻¹. Accordingly, one cannot extract any clear trends from this data nor select a particular structure. The capacitance data against SSA presented in Figure 1i (Table S1, Supporting Information) again shows no apparent trend across the different RGO samples. Instead, the values are seemingly randomly populated with a capacitance difference of more than 200 F g⁻¹ at any given value of a SSA of RGO material. Such a capacitance difference is also observed for a SSA change from 100 to 1000 m² g⁻¹. Such complexity means no meaningful structure-related capacitance that one can consider/understand to design RGO-based supercapacitors. Most of the data in Figure 1i lies between SSA and capacitance values in the range of 100 to 500 m² g⁻¹ and 100 to 300 F g⁻¹, respectively. Some variation in capacitance is expected due to differing degrees of oxidation/reduction of the GO/RGO structures (Figure 1a,b) that result in disproportional conductive, nonconductive, and oxygenated or other heteroatom functionalized graphene sp²/sp³ carbon components, and accessible porosity of the graphenic framework for facilitating charge storage and its dynamics.^[12–25,27–42,44–53] Other factors (Figure 1c; Table S1, Supporting Information) that can affect the overall capacitance performance include electrode preparation routes resulting in different mass-loadings and thicknesses (ultra-low mass loadings or ultrathin layers of active materials often show high capacities over thicker counterparts due to enhanced charge and mass transfer).^[53,54] The nature of the capacitance measurements/calculations also contributes to the variations in performances (Figure 1e–g). In general, the capacitance performance of the material is determined via CV and GCD tests, and capacity values deduced at very low scan rates or current densities or capacitances reported from an arch- or long tail-like discharge curves (e.g., red data in figures) usually overestimate the capacities by 50% to 100%.

Our work addresses the above ambiguities; and therefore, identifies clear methods for optimizing the efficient charge storage in RGO based networks. To this end, we produced a series of GO precursors with a carefully controlled degree of oxidation (C:O ratio), from very mild to high. Following this, a thermal-shock exfoliation of the GO samples was carried out under a wide range of temperatures (160 °C to 1000 °C) in a preheated fur-

nace. The thermal-shock exfoliated GO products (EGs) offered significant control over structural properties, porosities (SSA, pore size and distribution, and pore volume), alongside degree of reduction, sp²/sp³ carbon ratio, and residual oxygen functionality or C:O ratios. GO samples with a high degree of oxidation, synthesized by excess acid–salt mixtures in modified Hummer's method, showed a higher exfoliation degree compared with GO samples obtained in a typical Hummer's method or at lower acid–salt concentrations. Different electrode preparation routes, such as water and *N*-methyl-2-pyrrolidone (NMP) organic solution dispersion based drop and dip casting, and direct dry powder pressing onto glassy carbon and nickel foam substrate electrodes were carried out to understand and optimize charge storage capacities. All the measurements were performed in a three-electrode test system with 1 M KOH aqueous electrolyte. An unpredictable capacitance variation in the electrode structures fabricated from both water and NMP based EG-dispersions was observed and it was found that the capacitance largely depends on the substrate electrodes and surface binding. Interestingly, relatively high capacitance values (340 ± 10 F g⁻¹ at 0.5 A g⁻¹ vs 190 ± 20 F g⁻¹ in electrodes made from EG-dispersions) were observed in electrodes made with packed dry powder samples in compressed nickel foam that used no additives such as binder and conducting carbon black agents. The data from dry powder-based electrodes also show SSA governed capacity relationship with an impressive capacitance of 240 ± 10 F g⁻¹ at 1.0 A g⁻¹ for a given SSA of 800 ± 25 m² g⁻¹ due to the highly accessible electrode–electrolyte interface and strong EG–substrate interactions. Overall, our work offers clear insights into the origin of the large discrepancies in capacitance performance relationships of RGO based structures. Moreover, we demonstrate a simple and scalable processing route for producing extensively interconnected graphene networks via rapid thermal-shock exfoliation of GO with optimized oxidation (C:O ratio), promising for other energy storage applications such as high voltage and energy density organic and ionic liquid SCs as well as alkali-metal batteries.

2. Results and Discussion

Figure 2 shows the synthesis and processing of our GO and EG samples and their structural characteristics. GO samples with mild to intense (1–9) oxidation are represented with GO-1 to GO-9 and their thermally-shock exfoliated products as EG-1 to EG-9. The GO samples were examined under powder X-ray diffraction (PXRD) and X-ray photoemission spectroscopy (XPS), which indicate a controllably increased oxidation degree (Figure 2a,b,c; Figures S1 and S2 and Table S2, Supporting Information). The oxidation degree, that is, the oxygen content, was increased from 27.0 at% to >33.0 at% for GO-1 to GO-9. This is equivalent to a C:O ratio change from 2.67 to ≈2.0 for highly oxidized GO samples. PXRD patterns with (1 0 0) reflection in the 2θ region of 10° to 11° suggest a gradually increased interlayer distance with increasing oxidation from 0.74 to 0.82 nm. This is a significant change, more than doubling the spacing to that of 0.34 nm in the graphite starting material. The above results are in agreement with reported GO samples, noted in Table S1, Supporting Information; and thus, can represent different types of GO samples and for further processing to generate a range of RGO materials. Next, EG materials, were produced by thermal-shock exfoli-

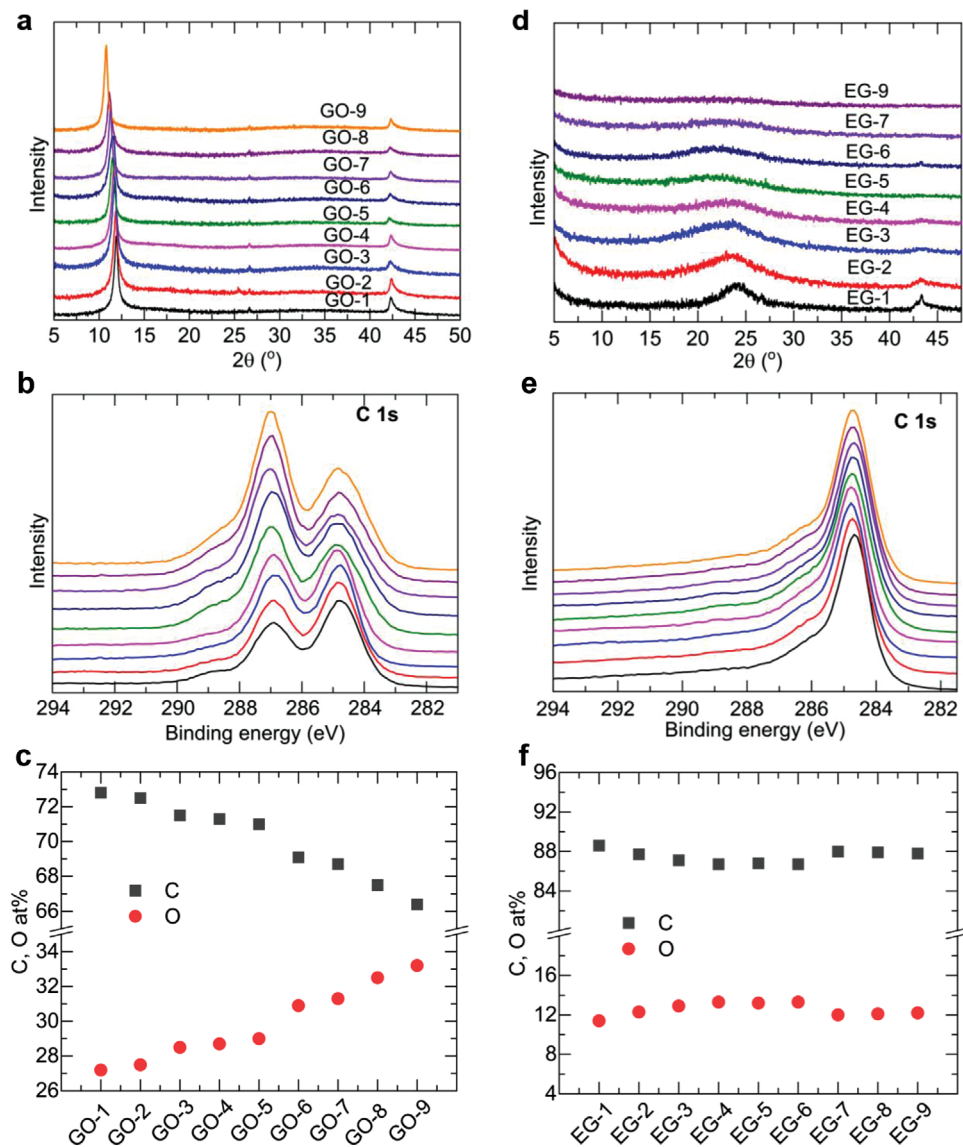


Figure 2. Structural characteristics of GO precursors and as-produced EG samples. a,d) PXRD patterns of GO and EG. b,e) XPS C 1s spectra of GO and EG. Same color code key applies for the data in (a), (b), and (e). c,f) XPD survey deduced C and O atomic concentrations in GO and EG.

ation at 300 °C, resulting in a destruction of their layered structure and reduction with significantly reduced oxygen functional groups (Figure 2d,e,f; Figure S3 and Table S3, Supporting Information). PXRD patterns of EG obtained from mildly oxidized GO show a weak graphitic feature with broader (2 0 0) and (1 0 0) reflections at $\approx 24^\circ$ and $\approx 43^\circ$ of 2θ values and corresponding d-spacing of 0.37 nm, indicating partial retention of the graphitic layered structure. However, this feature gradually weakened, fully disappearing in EG samples generated from highly oxidized GO, evidencing a more complete exfoliation of GO layers. As summarized in Table S3, Supporting Information, as-produced EG samples show oxygen content between 11.4 at% and 13.3 at% or with resultant C:O ratio between 6.5 and 7.8, indicating a high reduction degree as the C:O ratio is increased substantially from 2.0 for GO-9. Such reduction of the C:O ratio is comparatively higher than many RGO materials obtained via thermal, chemical,

or hydrothermal or combined reduction routes (see the literature summary in Figure 1b; Table S1, Supporting Information). Interesting porous networking features of the EG are observed from electron microscopy and porosity characterizations. For example, scanning and transmission electron microscopy (SEM and TEM respectively) images in **Figure 3** reveal gradually expanded and interconnected graphenic layered structures produced from GO-1 to GO-9 precursors of low to intensely oxidized forms. Clearly, EGs derived from low oxidized GO precursors (e.g., GO-1 to GO-3) result in mildly exfoliated or expanded structures, closely stacked layers in SEM and/or thick slabs like morphology in TEM images (Figure 3a,f), which is consistent with PXRD data (Figure 2d). In contrast, extensive exfoliation can be seen for the EG samples derived from highly oxidized GO materials. Here, it is worth mentioning that such exfoliation also produces greatly interconnected graphene networks. As shown in **Figure 4**, these

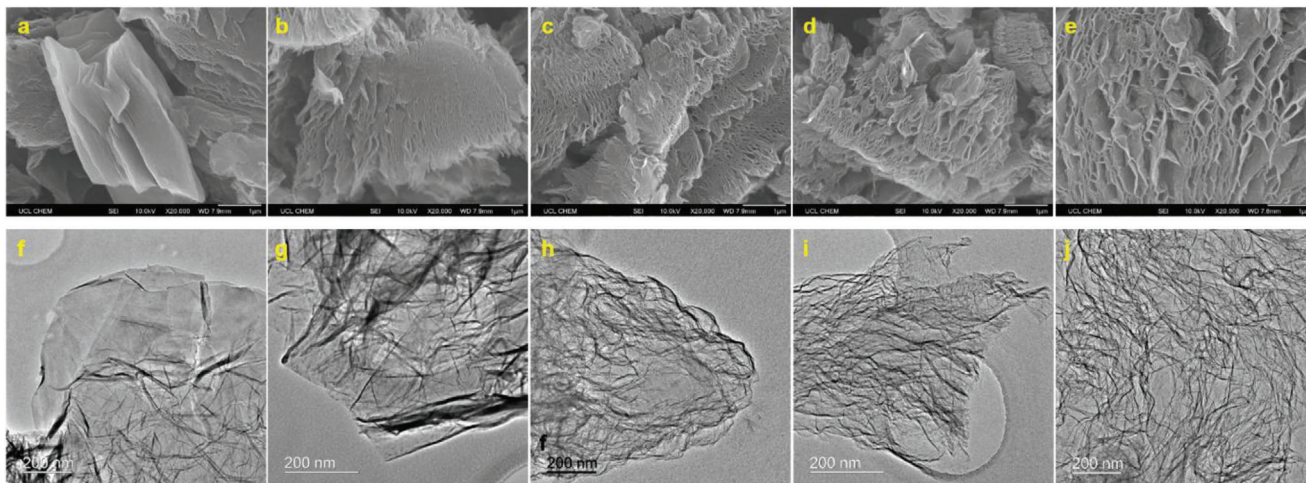


Figure 3. Surface and interface morphological characteristics of EG samples. SEM (top panel, with scale bar of 1 μm) and TEM (bottom panel) micrographs of a,f) EG-1, b,g) EG-2, c,h) EG-3, d,i) EG-6, and e,j) EG-9 samples.

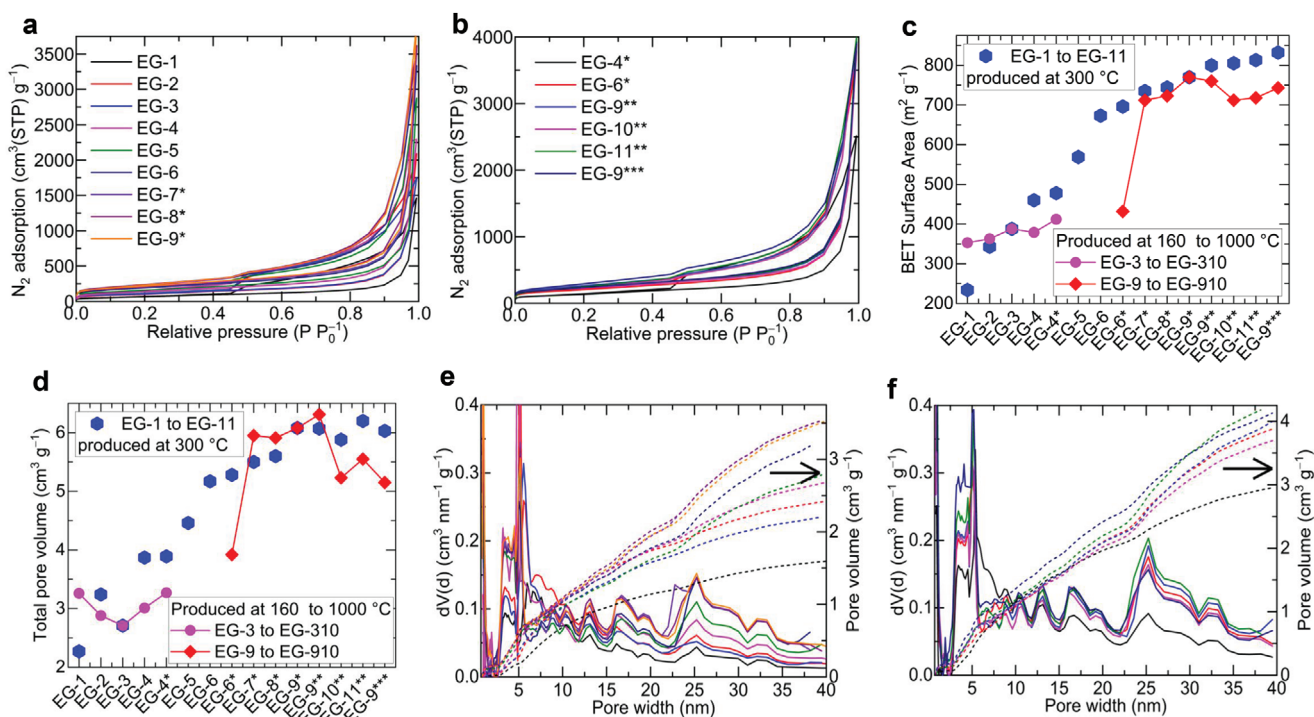


Figure 4. Porosity characteristics of EG samples. a,b) N_2 adsorption–desorption isotherms. c,d) Isotherm-deduced BET specific surface area and total pore volume. e,f) Pore-size distribution and pore volume (on the right axis) curves (the same color code key of (a,b) applies to (e) and (f), respectively).

EG porous networks exhibit high amounts of N_2 molecular adsorption capacities of 2000 to 4000 $\text{cm}^3 \text{g}^{-1}$ at -196°C (77 K) under relative pressure of 0.995. The qualitative behavior of N_2 adsorption–desorption isotherm data suggests a highly hierarchical porous structure with porosity spanning across micro-porous (with pore widths of below 2 nm), meso-porous (pore widths across 2 to 50 nm), and macro-porous (pore widths of over 50 nm) regions. The SSA values deduced by the Brunauer–Emmett–Teller (BET) method and the total pore volume by N_2 adsorbed

amounts at a relative pressure of 0.995 indicate a gradual increase in the porosity (Figure 4c,d; Table S4, Supporting Information) for EG materials, derived from GO precursors of increased oxidation degree. Pore size and pore size distribution data (Figure 4e,f), obtained by applying quenched solid density functional theory (QSDFT) with slit/cylindrical pore fitting models to the desorption isotherms also suggest continuously enhanced pore population across all three porosity regimes, in agreement with increased exfoliation, supported by XRD (Figure 2d) and SEM/TEM

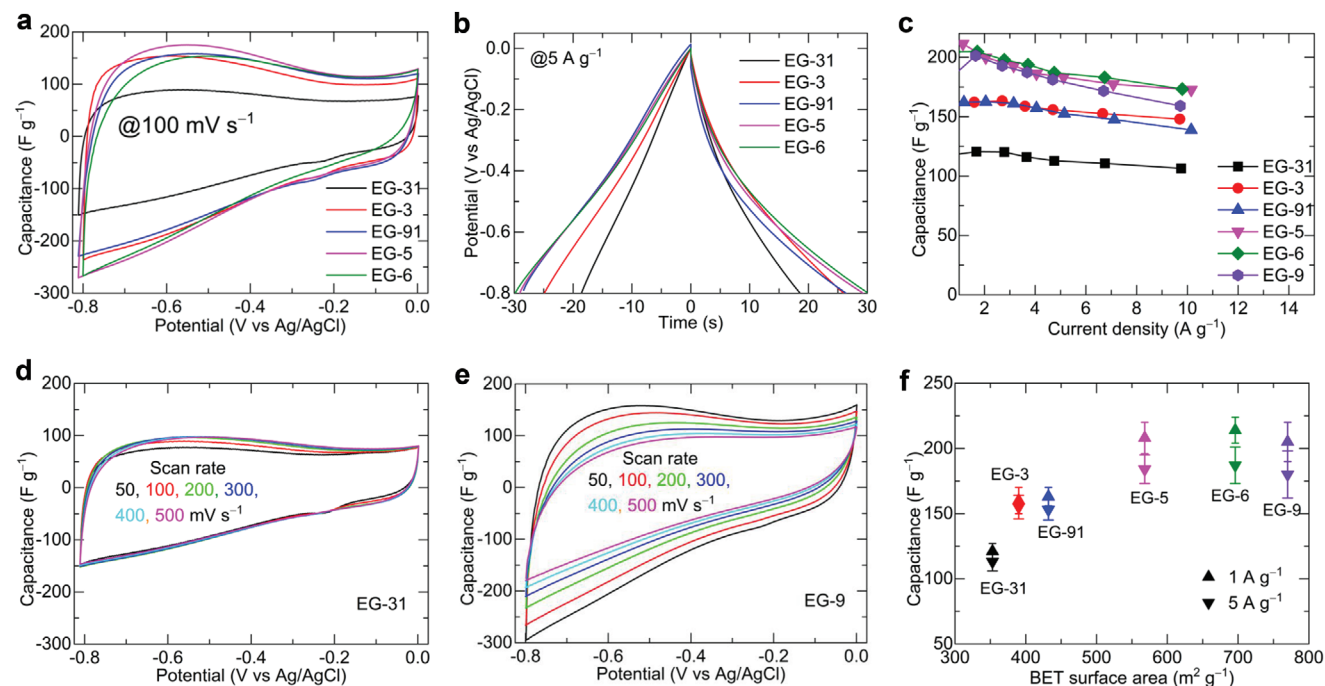


Figure 5. Supercapacitor characteristics of EG-water dispersion drop-casted GCE discs. a) CV curves at a scan rate of 100 mV s^{-1} . b) GCD curves at current density of 5.0 A g^{-1} . c) Rate capacitance curves deduced from discharge data of GCD curves. d,e) CV curves of EG-3 and EG-9 at scan rates between 50 and 500 mV s^{-1} . f) Specific surface area dependence of specific capacitance values, derived from discharge data of GCD curves at current density of 1.0 and 5.0 A g^{-1} .

(Figure 3) data. Together, these results demonstrate that more oxygen functional groups in the GO structures can result in efficient exfoliation and highly networked open porous structures.

Structurally, GO comprises stacked layers with interlayer hydroxyl or water molecules and sudden volatility or decomposition of edge and interlayer bound carboxyl and hydroxyl/water molecules under rapid heat creates an enormous pressure build-up between layers and eventually leads to exfoliation/detonation of the GO structure.^[55] The decomposition of carboxylic and epoxide groups during the exfoliation process offers greatly reduced EG products of extremely open pore framework structure. Here, it is worth mentioning that the SSA values of more than $800 \text{ m}^2 \text{ g}^{-1}$ in EG materials produced under optimal conditions in this work are comparatively higher than RGO structures in the literature (Figure 1i; Table S1, Supporting Information), which are mostly limited to $500 \text{ m}^2 \text{ g}^{-1}$. In addition, to establish an optimal mild exfoliation temperature, two representative GO samples, GO-3 and GO-9, are subjected to a range of exfoliation temperatures between $160 \text{ }^\circ\text{C}$ and $1000 \text{ }^\circ\text{C}$. This process suggests a temperature of $300 \text{ }^\circ\text{C}$ as an optimum at which efficient exfoliation occurs in less than 5 min. GO exfoliated at lower or higher temperatures offers no advantage in terms of exfoliation; higher temperature can reduce the exfoliation time; for example, exfoliation can be achieved in less than a minute at $\geq 800 \text{ }^\circ\text{C}$ and GO subjected at temperatures of $160 \text{ }^\circ\text{C}$ reveals a partial or inefficient exfoliation, which also takes a longer time of more than 20 min. The relevant experimental and structure-related properties, such as XPS and porosity deduced data are summarized in Figure 4c,d; Figures S4 and S5 and Tables S5 and S6, Supporting Information. The mild exfoliation yields a reduced porosity in the sam-

ples; however, exfoliation at all other higher temperatures offers similar EG structures with nearly identical reduction and porosity characteristics, meaning that a temperature of $\approx 300 \text{ }^\circ\text{C}$ is optimal to generate EG with efficient exfoliation and reduction. Overall, the results support the conclusion that the exceptional porosities in EG samples are obtained by not only optimizing the GO precursors but also by exploiting the exfoliation conditions, such as temperature and precursor loading amounts.

These as-produced EG samples, without carrying out any further reduction treatments such as high temperature thermal or hydrothermal/solvothermal annealing routes, were directly screened for their supercapacitive charge storage performance. All the samples were characterized in a three-electrode system containing 1 M KOH alkaline electrolyte by performing CV and GCD tests at different potential scans and current densities, respectively. In each case, the samples had been tested multiple times. Figure 5 shows the capacitance characteristics of EG samples measured on water-EG dispersion deposited glassy carbon electrode (GCE) discs. Briefly, a dispersion was prepared via ultrasonication of EG (2.00 g) in deionized water (2.0 mL) and Nafion binder solution. The finely water-dispersed EG was drop-casted onto a GCE disc for a dry sample mass loading of $\approx 0.01 \text{ mg}$ or areal mass loading equivalent of $\approx 0.14 \text{ mg cm}^{-2}$. The quasi-rectangular CV curves and quasi-triangular GCD curves of these samples—typical features of RGO samples or other microporous inorganic networks—evidence impressive capacitance values, reaching higher than 200 F g^{-1} at a high current density of 1.0 A g^{-1} . An improvement in capacity for samples EG-3 to EG-9 can be seen. However, there is a clear inconsistency in their capacitance values with respect to the rate capacitance and samples with

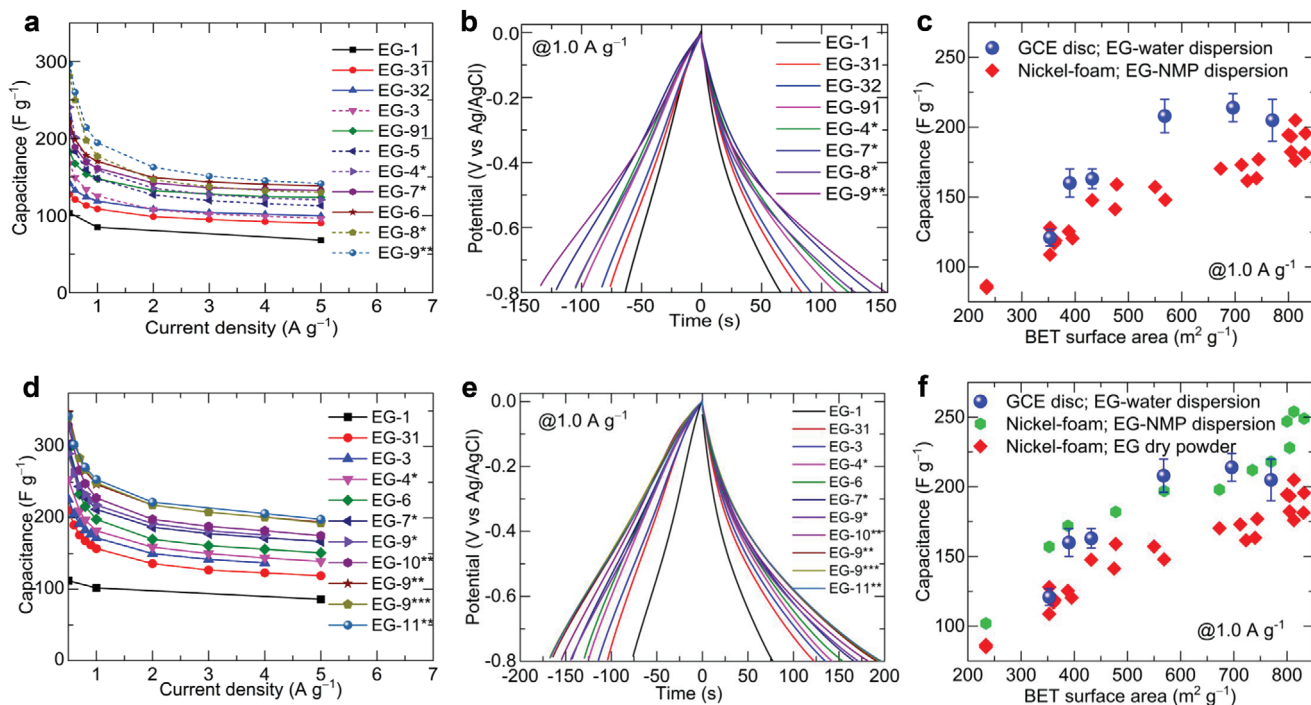


Figure 6. Supercapacitor characteristics of EG-NMP dispersion dip-casted nickel foam electrodes (top panel) and electrodes made directly from EG-dry powder sample on a nickel foam (bottom panel). a,d) Rate capacitance curves deduced from discharge data of GCD curves. b,e) GCD curves at current density of 1.0 A g^{-1} . c,f) Specific surface area dependence of specific capacitance values, derived from discharge data of GCD curves at current density of 1.0 A g^{-1} .

increased porosity (surface area). The rate capacitance at higher current densities seems to fall rapidly in the highest SSA EG (e.g., EG-9) samples (Figure 5c). Such variation is also observed in their CV curves; for instance, a continuously reduced area under the CV curves of EG-6, EG-9, and EG-91 at increased scan rates indicates rapidly reduced capacitance compared to more or less identical CV curves of EG-3 or EG-31 samples under similar scan rates (Figure 5d,e; Figure S6, Supporting Information). A noteworthy irregularity is seen in their capacitance plotted against the SSA of the samples (Figure 5f). For example, similarly reduced (i.e., similar C:O ratio, in Table S3, Supporting Information) EG samples with a SSA of 350, 430, and $570 \text{ m}^2 \text{ g}^{-1}$ exhibit capacitance of 120 ± 6 , 160 ± 7 , and $208 \pm 12 \text{ F g}^{-1}$, respectively at 1.0 A g^{-1} , yielding an approximately linear relationship. Whereas, EG-6 and EG-9 samples with higher SSA of 700 and $770 \text{ m}^2 \text{ g}^{-1}$, respectively, show no further improvement in capacities, and observed values of 214 ± 10 and $205 \pm 15 \text{ F g}^{-1}$ are lower than expected ones as per the SSA-capacity linear relation. A rapid capacitance drop in the cyclic test (Figure S6, Supporting Information) and sample leaching out into electrolyte is also visibly observed during tests, particularly in the highly porous samples deposited on GCE discs.

These observations motivated us to undertake further experiments to understand the true structure–performance relationship, for which the samples are extensively screened by performing measurements using newly fabricated nickel foam based electrodes (which can offer higher surface area and accessibility for both sample deposition and electrolyte access). In these experiments, the EG samples were dispersed in NMP organic solution, instead of water for an easy and efficient dispersion,

with polyvinylidene fluoride (PVDF) binder via ultrasonication following dip-casting onto pre-cleaned nickel foam and dried at $180 \text{ }^\circ\text{C}$ in an oven under ambient air. The electrode casting was optimized for solution concentration and mass loading (achieved between 0.7 and 1.7 mg cm^{-2}) onto centimeter wide nickel foam strips. As shown in Figure 6a, the rate capacitance curves derived from GCD curves demonstrate significantly enhanced capacities, reaching $280 \pm 20 \text{ F g}^{-1}$ at 0.5 A g^{-1} , compared to a limited capacity of $214 \pm 10 \text{ F g}^{-1}$ from GCE disc tests (in Figure 5). Another noteworthy observation is that the capacity at 1.0 A g^{-1} tends to exhibit an increased capacitance relation against the SAA of EG samples (Figure 6b,c). Here, somewhat lower capacitance values are obtained compared with the results of the GCE discs. This reduction can be linked to a high mass-loading of $\times 100$ that of GCE (i.e., 1.00 mg compared to 0.01 mg , or up to $\times 10$ of areal mass loading, $\approx 1.50 \text{ mg cm}^{-2}$ to $\approx 0.14 \text{ mg cm}^{-2}$) that limits the electronic and ionic mass transfer kinetics.^[12,13,53] The nickel foam based EG electrodes also offer improved cyclic stability over GCE based EG under long-term operation (Figure S7, Supporting Information) and a capacitance drop of less than 10% in $\approx 10\,000$ repeated charge–discharge cycles at a high current density of 5.0 A g^{-1} . Although the data in Figure 6c seems to establish a definite SSA-governed capacity trend, it should be noticed that the capacity of the same nominal sample (prepared multiple times) and/or samples of similar SSA (i.e., a difference of less than $50 \text{ m}^2 \text{ g}^{-1}$ or with an error margin of $\pm 25 \text{ m}^2 \text{ g}^{-1}$) show a capacity variation of up to 40 F g^{-1} (or $\pm 20 \text{ F g}^{-1}$). For some electrode structures, this variation can be linked to dissimilarity in their mass loading (some electrodes were measured with lower mass loadings of

$\approx 0.80 \text{ mg cm}^{-2}$ and others contain more than 1.2 or up to 1.70 mg cm^{-2} for EG samples of lower porosity). Another factor for this is variation manifests in their rate capacitance, which is shown in Figure 6a. Here, it is worth noting that although most of the samples exhibit identical rate behavior (solid line data curves), some of the rate capability drops faster (identified by thick dotted line data curves) than others. This rapid capacitance loss or poor rate capacitance is seen more often in the highly porous EG samples, possibly due to a weaker interaction between highly porous EG and nickel foam electrode with such graphene flakes even visibly detaching from the electrode to fall into the electrolyte. To improve adhesion, more binder was added to the NMP-EG dispersion for the highly porous samples, and the ultrasonication time was extended as well as pressing the electrode structures under 1 to 5 tonnes of pressure using a hydraulic press. These adaptations did not result in any noticeable improvement in their capacitance performance. It is further observed that a large batch of the NMP-EG dispersion prepared in a vial directly dried at 180°C under ambient air retained a significant amount of NMP (about 30% by mass) in the structure, which is identified by weighing samples before dispersing in NMP and after drying NMP-EG dispersion. The sample dried at 250°C under dynamic vacuum overnight in a porosity analyzer also showed retention of a considerable amount of NMP residue and the porosity measurement on this large batch of NMP-EG dried sample showed a comparatively low SSA with respect to its EG counterpart. Therefore, it indicates that the charge storage performance of highly porous EG samples could be further improved if electrodes were fabricated using other routes or avoiding especially NMP but also water and organic solvent dispersion based casting methods on current collector substrates.

By taking advantage of highly interconnected open networks and low-dense fluffy-like EG materials (Figure S8, Supporting Information, and from the electron microscopic and porosity data in Figures 3 and 4), electrodes were fabricated directly from dry powders of as-produced EG samples, without the use of binder or additional conducting carbon components. For this, EG powder of 1.00 mg was spread on to a piece of flattened nickel foam over which another piece of flattened nickel foam was pressed at 1.0 tonnes of pressure using a hydraulic press to form a sandwich/pouch-like assembly to prevent sample leaking out into the electrolyte. As shown in Figure 6d, the rate capacitance curves obtained from these newly fabricated electrodes exhibit identical behavior among the samples and offer substantially enhanced capacities, reaching $340 \pm 10 \text{ F g}^{-1}$ at 0.5 A g^{-1} . This is an increase of more than 130 and 50 F g^{-1} over the electrodes fabricated from water- and NMP-based EG dispersions, respectively. Moreover, the overall capacities deduced at 1.0 A g^{-1} in all the EG samples are about 20% higher than the values obtained from the NMP-EG dispersions based electrodes (Figure 6e,f). This confirms that the dry powder pressed electrodes are free from binder and NMP residue elements, and in addition, there is a strong EG sample and current collector nickel foam interaction; thus, readily facilitating extensive interfacial surface for charge storage and electron transfer reactions.^[12–15] It is also noted that most of the dry compressed EG samples are firmly enclosed and bound to the nickel foam; thus, there is greatly reduced sample loss into the electrolyte. Other plate or foil-type enclosures, into

which dry powders are pressed, are promising, as discussed in the literature.^[15]

The critical analysis, along with extensive data accumulated from numerous samples, reveals a large variation in the capacitance values measured on electrode structures fabricated using different methods. Together these data can reconcile the large discrepancies in the capacities of RGO materials presented in Figure 1. The capacitance performance of EG samples in this study follows their structure-relevant features of exfoliation, reduction degree, and porosity. That is, as in this case, the samples with similar C:O ratio have a capacitance that is proportional to SSA (Figure 6). As presented in Figure 1b, the literature data of RGO materials mainly fall between capacities of 100 and 300 F g^{-1} and SSAs of between 100 and $500 \text{ m}^2 \text{ g}^{-1}$. Here, the high capacitance values in Figure 1 can be linked to a lower reduction with a C:O ratio of less than 6.0 (e.g., hydrothermally reduced/etched RGO structures) and/or heteroatom dopants and micro-porosity (e.g., in RGO films with ultra-small/slit-like pores to micro-pores) in the RGO samples, and such factors induce a significant amount of pseudo-capacitance.^[13,19–25,29,43,56] These combined properties actively enhance EDLC and pseudo-capacitance significantly and contribute to boosting the total capacitance. In this context, it is worth noting that in many cases, porous graphene structures in the literature have been developed with an extended post-synthesis chemical manipulation of as-synthesized GO. Notably, for instance, as-synthesized GO has been subjected to prolonged ultrasonication to achieve an exfoliated GO suspension; then, further processed by hydro-/solvo-thermal curing, vacuum filtration or cast into templates of mesostructured foams followed by reduction either with chemical and/or thermal routes (see details in Table S1, Supporting Information). Nevertheless, the high capacitance values of 280 ± 20 to $340 \pm 10 \text{ F g}^{-1}$ at 0.5 A g^{-1} in EG samples in this work are higher than most of the RGO based structures in the literature and superior to direct solid-state thermal-/microwave-shock exfoliated and plasma reduced graphene counterparts,^[28,29,51,57–67] which typically show capacitance of $< 250 \text{ F g}^{-1}$ (Figure S9, Supporting Information). Such an improvement of up to 40% suggests that despite using similar techniques, our optimized synthesis and processing conditions can lead to significant enhancement in their final device performance. Another interesting point to note is that the capacitance values of $240 \pm 10 \text{ F g}^{-1}$ at 1.0 A g^{-1} in EG samples are comparatively superior, at most more than 50 F g^{-1} or $\approx 100 \text{ F g}^{-1}$, to typical mesoporous carbon nanostructures of identical or far higher surface areas between 1000 and $3000 \text{ m}^2 \text{ g}^{-1}$.^[9,11,15–19,68–75] For example, NPCs generated via salt or organic templates and after high temperature pyrolysis or activation with a specific surface area of $800 \text{ m}^2 \text{ g}^{-1}$ show a capacitance of 200 F g^{-1} at 0.5 A g^{-1} . Moreover, the SSA-normalized capacitance values of EG samples presented here spanning from 20 – $45 \mu\text{F cm}^{-2}$ are also relatively higher than most of the other extremely high surface area carbon based materials in the literature,^[9,11,75] usually less than $10 \mu\text{F cm}^{-2}$ (Figure S10, Supporting Information). Highly microporous NPCs can offer enhanced areal capacities but area limit to under $20 \mu\text{F cm}^{-2}$.^[9,11,75] Such superior capacitance values in EG can be directly attributed to the residual oxygen groups associated with enhanced electrode–electrolyte interaction^[74] (efficient wetting), extensive meso-porosity, hierarchical pore networking,

and conducting samples. Therefore, our results show that the graphene/carbon related materials can be tuned to achieve high performance electrochemical energy storage and conversion and guest molecular capture/storage.

3. Conclusion

This study was designed to demonstrate and understand the large discrepancies in capacitance data for RGO based structures generated under nominally identical and/or mild reduction processes. For this, we measured over 40 RGO based electrodes that are fabricated from over 20 RGO materials via three different processing methods, via solution (aqueous and organic) casting and compressed powders onto glassy carbon and nickel foam supports. Electrochemical tests on these electrodes made from different methods showed different capacitance values with difference of more than 100% or capacitance change from 190 ± 20 to $340 \pm 10 \text{ F g}^{-1}$; thus, linking the capacitance variation to difference in electrode production. In addition, our work also reveals a typical SSA governed capacitance with a directly proportional dependence of charge storage capacity on SSA of RGO structures with an identical degree of reduction. Such a relationship could not be derived from the literature data, which showed a capacitance difference of up to 250 F g^{-1} for a given SSA in RGO. Overall, the significant difference in the C:O ratio, along with heteroatom dopants and electrode preparation routes yields a difference in mass loading, structure packing, slit-like pores or micro-porosity to meso-porosity, accessible electrode–electrolyte interface to influence electrochemical charge storage, mass and electron transfer phenomenon. Optimized GO samples synthesized by controlling the oxidation degree, treated at $\leq 300 \text{ }^\circ\text{C}$ for a few minutes readily yield RGO networks with a residual oxygen content of $< 13 \text{ at}\%$, along with exceptionally interconnected hierarchical porosity with a specific surface area of $800 \text{ m}^2 \text{ g}^{-1}$ and pore volume exceeding $6.0 \text{ cm}^3 \text{ g}^{-1}$. This structural property is ideal for accepting high amounts of guests and for their mass/electron transfer reactions readily. Moreover, this synthesis route is highly scalable.

4. Experimental Section

Materials: All chemicals were used as received, commercial grade. Synthetic graphite powder of $< 20 \text{ micron}$ (Sigma–Aldrich); potassium permanganate of $\geq 99.0\%$ (Sigma–Aldrich); potassium hydroxide of $\geq 86\%$, puriss, pellets (Sigma–Aldrich); sulfuric acid of $95\text{--}97\%$, puriss (Sigma–Aldrich); phosphoric acid of $\geq 85 \text{ wt}\%$, ACS reagent (Aldrich); hydrogen peroxide solution of $34.5\text{--}36.5\%$ (Sigma–Aldrich); hydrochloric acid of 35% , technical 38% (VWR); polyvinylidene fluoride (PVDF) powder (Sigma–Aldrich); N-methyl-2-pyrrolidone (NMP) of 99% (Sigma–Aldrich); Nafion (5% solution, Sigma–Aldrich); N_2 gas of research grade purity, BOC gases, UK; nickel foam for battery, 1.6 mm thick, surface density: 350 g m^{-2} , area: 0.30 m^2 (MTI Corporation).

Synthesis of GO Samples: GO-1 to GO-11 samples of different degrees of oxidation were prepared by Hummer's and modified Hummer's methods. GO-3 sample was synthesized as follows; graphite powder, typically 10 g was stirred with cold concentrated H_2SO_4 (230 mL at $0 \text{ }^\circ\text{C}$). KMnO_4 (30 g) was added to the suspension slowly to prevent a rapid rise in the temperature (less than $20 \text{ }^\circ\text{C}$). The solution underwent a color change at this point from black to a very dark green. After removal of the ice-bath, the mixture was stirred at room temperature for another 2 h . Deionized water (230 mL) was slowly added to the reaction vessel to keep the temperature under $98 \text{ }^\circ\text{C}$. The diluted suspension was stirred for an additional 15 min

and further diluted with DI water (1.4 L) before adding H_2O_2 (100 mL). Upon addition, vigorous foaming occurred and the solution turned brown. The mixture was stirred for 2 h at room temperature and left overnight. The product settled at the bottom was separated from the excess liquid by decantation followed by centrifugation. The product was washed by centrifugation until the pH reached neutral and then freeze-dried to obtain a final product. GO-1, GO-2, and GO-4 were prepared under similar conditions but with a change in graphite: KMnO_4 weight ratio, for example, in 1:1, 1:2, and 1:4 g g^{-1} , respectively. GO-6 sample was synthesized as follows; graphite powder (2.0 g) was added to 9:1 mixture of concentrated H_2SO_4 (45 mL) and H_3PO_4 (5 mL) under stirring at cold ($\approx 0 \text{ }^\circ\text{C}$). KMnO_4 (12.0 g) was then added slowly to prevent the sudden temperature rise, not more than $10 \text{ }^\circ\text{C}$. The solution became a very dark green. The reaction mixture was then heated to $50 \text{ }^\circ\text{C}$ and left for 3 h under stirring. At this point, the mixture turned into a brown paste. Deionized water (240 mL) was added very slowly, again to prevent a sudden temperature rise of highly exothermic reaction (water to a concentrated acid) to the mixture, which turned to a dark brown color. The reaction mixture was left to stir for several minutes. In the final step, H_2O_2 (16 mL) was slowly added to the solution causing vigorous foaming and a color change to a bright yellow. The solution was stirred for another 30 min at a warm state ($50 \text{ }^\circ\text{C}$) and left to settle overnight at room temperature. The solid product was separated from the excess liquid by centrifugation followed by decantation. The product was then washed in dilute HCl (3.4% , 750 mL) to remove any remaining salts, followed by further washing in DI water until the washings were pH neutral. The GO-6 sample was obtained after being freeze-dried for ≈ 7 days. GO-7, GO-8, and GO-9 were prepared under similar conditions as GO-6 but with a change in reaction (graphite + acid + KMnO_4 mixture) heating temperature and heating time; the mixture was stirred for 8 h at $50 \text{ }^\circ\text{C}$ for GO-7 and overnight for GO-8, and 6 h at $80 \text{ }^\circ\text{C}$ for GO-9. GO-5, GO-10, and GO-11 were prepared under similar conditions as GO-6 but with a change in graphite: KMnO_4 weight ratio of 1:5, 1:8, and 1:10 g g^{-1} , respectively and reaction (graphite + acid + KMnO_4 mixture) heating time set to 6 to 8 h under stirred conditions at $50 \text{ }^\circ\text{C}$.

Synthesis of EG Samples: Thermal exfoliation was carried out at $300 \text{ }^\circ\text{C}$ (unless specified) in a pre-heated vertical tube furnace. 0.2 to 2.0 g of GO sample was charged into a glass tube of 1.5 in. diameter and 12 in. length under ambient air. The tube was then covered with a paper towel and placed in a furnace. From this point, the exfoliation could be seen in ≈ 2 to 5 min ; some of the samples were exfoliated in multiple steps. Thus, the sample tube was still left in a furnace for additional 2 min for completing the process. After this, the sample tube was removed from the furnace and left on the bench to cool down. Exfoliated samples were collected for further characterization. No further chemical treatment was performed. The as-exfoliated samples were examined straight away for characterization including gas adsorption and processing for electrode materials. EG-1 to EG-6 samples were produced using 2.0 g GO in a single batch. EG-4*, EG-6* to EG-9* samples were produced using 1.0 g GO in a single batch. EG-9** to EG-11** samples were produced using 0.5 g GO in a single batch. EG-9*** sample was produced using 0.2 g GO in a single batch. EG-31 to EG-310 and EG-91 to EG-910 samples were produced via thermal-shock exfoliation described above using 1.0 g of GO-3 and GO-9 precursors in a single batch and under different pre-heated temperatures of $160 \text{ }^\circ\text{C}$, $200 \text{ }^\circ\text{C}$, $250 \text{ }^\circ\text{C}$, $300 \text{ }^\circ\text{C}$, $400 \text{ }^\circ\text{C}$, $600 \text{ }^\circ\text{C}$, $800 \text{ }^\circ\text{C}$, and $1000 \text{ }^\circ\text{C}$. At $160 \text{ }^\circ\text{C}$ and $200 \text{ }^\circ\text{C}$, exfoliation took more than 10 and up to 30 min , whereas at or above $800 \text{ }^\circ\text{C}$, the process was completed rapidly in about a minute or less.

Characterization for GO and EG Samples: Powder X-Ray diffraction (PXRD, Cu $K\alpha$ radiation, Thermo Scientific) was carried out in the scan range of $2\theta = (2\text{--}60)^\circ$ and at a step size of 0.01° . X-ray photoemission spectroscopy (XPS, Al-K-alpha, Thermo Scientific) data, scanning electron microscopy (SEM, Jeol), and transmission electron microscopy (TEM, Jeol) measurements were carried out on the samples supported on a carbon tape or a carbon-coated copper TEM grid. N_2 adsorption–desorption isotherms in the pressure range of vacuum to 0.995 of relative pressure were measured at 77 K using a Quantachrome Autosorb-iQC. The specific surface area was determined from the N_2 isotherm, according to the Brunauer–Emmett–Teller (BET) method. QSDFT (quenched solid density

functional theory, available within the Quantachrome ASIQwin isotherm analysis software) method with slit/cylindrical pores (≤ 50 nm) was applied to obtain a pore-size distribution and cumulative pore volume. The total pore volume was estimated from the amount of N_2 adsorbed at a relative pressure, P/P_0^{-1} of ≈ 0.995 . The samples were initially degassed at 180°C for up to 24 h prior to the actual adsorption isotherm measurements.

Fabrication of Supercapacitor Electrodes: Working electrodes were prepared via three different methods of 1) water dispersion and drop casting on to a GCE disc; 2) NMP dispersion and dip casting onto a nickel foam; and 3) direct dry powder packing in a nickel foam. Water dispersion and drop-casting method were obtained as follows; the active EG material of 2.00 mg for dry weight was dispersed in a total 2 mL solution consisting of 20–100 μL of Nafion binder (high amount of between 50 and 100 μL was used for highly porous EG samples) under sonication. The sonication was carried out for up to an hour or more to get a uniform dispersion ink. Out of this, 10 μL was micropipetted and dropped on to a glassy carbon electrode (GCE) disc followed by drying at 60°C in an oven prior to the electrochemical tests. This yield showed a fixed EG mass loading deposition of ≈ 0.01 mg (or 0.14 mg cm^{-2}) on a 3 mm diameter (or area of 0.0707 cm^2) GCE disc. NMP dispersion and dip-casting method were obtained as follows; the active EG material of 2.00 mg for dry weight was dispersed in a certain amount of NMP (1 to 2 mL depending on the EG porosity) organic solution consisting of 10 wt% of PVDF binder (up to 20 wt% also used for highly porous EG samples; all to make a materials weight ratio of 90:10 or up to 80:20) under sonication. The sonication was carried out for up to an hour or more to get uniform dispersion ink. The pre-cleaned (with hot HCl acid under sonication followed by washing and drying) nickel foam pieces (of 1 cm width and 3 cm long) were dipped into ink and dried at 180°C in an oven under ambient air. Direct dry powder packing in a nickel foam was obtained as follows; 1.00 mg of EG materials (with 0.01 mg accuracy) powder directly spread uniformly onto a 1 cm \times 1 cm area of pre-cleaned and hand flattened 1 cm \times 3 cm nickel foam strips and sealed into a pouch-like cell with another piece of nickel foam and compressed at 1.0–1.5 tonne of pressure for 1 min.

Electrochemical Tests of Electrodes: All electrochemical tests were carried out using an Autolab (Metrohm) electrochemical workstation, by a three-electrode method. Prefabricated EG-based GCE discs or nickel foam strips were used as working electrodes, and (1 cm \times 1 cm) Pt and Ag/AgCl/saturated KCl as counter and reference electrode, respectively in 1 M KOH electrolyte at room temperature. All the electrochemical test results were reported with respect to the reference, Ag/AgCl. Before actual measurements, the electrode was subjected to several CV cycles at a voltage-sweep rate of 100 mV s^{-1} until a stable CV was obtained. Then, the actual CV tests were conducted at different scan rates of 10 to 500 mV s^{-1} in a fixed potential range of -0.8 to 0.0 V. The charge–discharge curves with lower and upper and cut-off potentials of -0.8 and 0.0 V, respectively were recorded at a wide range of discrete applied current densities between 0.5 and 10.0 A g^{-1} . Long-term cyclic stability tests were conducted with multiple charge–discharge cycles of over 10 000 cycles at a constant applied current density of 5.0 A g^{-1} . The specific gravimetric capacitance (F g^{-1}) was calculated on the basis of charge–discharge curves at different current densities using the following equation: $C = (I \times \Delta t) / (m \times \Delta V)$, where C is the galvanostatic specific capacitance (F g^{-1}), I is the discharge current (A), m is the mass of the electrode material (g), Δt is the discharge time (s), and ΔV is the operating discharge potential window (V).

Supporting Information

Supporting Information is available from the Wiley Online Library or from the author.

Acknowledgements

This work was supported by EPSRC (grants of EP/R511638/1, EP/K021192/1, EP/S018204/2, EP/R023581/1, EP/W03395X/1,

EP/W033321/1) and Science Specialty Program of Sichuan University (Grant. No. 2020SCUNL210). The Royal Academy of Engineering is acknowledged for the financial support of P.R.S. (CIET1718-59) and D.J.L.B. (RCSR2021/13/53) under the Research Chairs and Senior Research Fellowships scheme. D.J.L.B. acknowledges the National Physical Laboratory (NPL) and HORIBA MIRA for the support of his RAEng Research Chair. J.G. acknowledges the Fundamental Research Funds for the Central Universities (2021SCU12116).

Conflict of Interest

The authors declare no conflict of interest.

Data Availability Statement

The data that support the findings of this study are available from the corresponding author upon reasonable request.

Keywords

electrode fabrication methods, graphene materials, structure–performance relationships, supercapacitors

Received: November 24, 2022

Revised: January 10, 2023

Published online:

- [1] J. Chen, P. S. Lee, *Adv. Energy Mater.* **2021**, *11*, 2003311.
- [2] P. Simon, Y. Gogotsi, *Nat. Mater.* **2020**, *19*, 1151.
- [3] H. Shao, Y. C. Wu, Z. Lin, P. L. Taberna, P. Simon, *Chem. Soc. Rev.* **2020**, *49*, 3005.
- [4] Q. Dou, H. S. Park, *Energy Environ. Mater.* **2020**, *3*, 286.
- [5] A. Dutta, S. Mitra, M. Basak, T. Banerjee, *Energy Storage* **2023**, *5*, e339.
- [6] X. Wang, M. Salari, D. Jiang, J. C. Varela, B. Anasori, D. J. Wesolowski, S. Dai, M. W. Grinstaff, Y. Gogotsi, *Nat. Rev. Mater.* **2020**, *5*, 787.
- [7] F. Han, O. Qian, G. Meng, D. Lin, G. Chen, S. Zhang, Q. Pan, X. Zhang, X. Zhu, B. Wei, *Science* **2022**, *377*, 1004.
- [8] J. Yin, W. Zhang, N. A. Alhebshi, N. Salah, H. N. Alshareef, *Small Methods* **2020**, *4*, 1900853.
- [9] S. Gadipelli, C. A. Howard, J. Guo, N. T. Skipper, H. Zhang, P. R. Shearing, D. J. L. Brett, *Adv. Energy Mater.* **2020**, *10*, 1903649.
- [10] S. Li, X. Song, X. Wang, C. Xu, Y. Cao, Z. Xiao, C. Qi, M. Wu, Z. Yang, L. Fu, X. Ma, J. Gao, *Carbon* **2020**, *160*, 176.
- [11] S. Gadipelli, Z. Li, Y. Lu, J. Li, J. Guo, N. T. Skipper, P. R. Shearing, D. J. L. Brett, *Adv. Sci.* **2019**, *6*, 1901517.
- [12] Z. Li, S. Gadipelli, H. Li, C. A. Howard, D. J. L. Brett, P. R. Shearing, Z. Guo, I. P. Parkin, F. Li, *Nat. Energy* **2020**, *5*, 160.
- [13] Z. Li, S. Gadipelli, Y. Yang, G. He, J. Guo, J. Li, Y. Lu, C. A. Howard, D. J. L. Brett, I. P. Parkin, F. Li, Z. Guo, *Energy Storage Mater.* **2019**, *17*, 12.
- [14] Z. Li, S. Gadipelli, Y. Yang, Z. Guo, *Small* **2017**, *13*, 1702474.
- [15] P. Pachfule, D. Shinde, M. Majumder, Q. Xu, *Nat. Chem.* **2016**, *8*, 718.
- [16] Y. Long, X. An, H. Zhang, J. Yang, L. Liu, Z. Tian, G. Yang, Z. Cheng, H. Cao, H. Liu, Y. Ni, *Chem. Eng. J.* **2023**, *451*, 138877.
- [17] H. Zhang, Y. Liu, C. Lin, Y. Zhang, *ChemElectroChem* **2022**, *9*, 202200801.
- [18] P. Ren, D. Wu, T. Wang, P. Zeng, D. Jia, *J. Power Sources* **2022**, *532*, 231072.
- [19] J. S. M. Lee, M. E. Briggs, C. C. Hu, A. I. Cooper, *Nano Energy* **2018**, *46*, 277.

- [20] S. Panda, K. Deshmukh, S. K. K. Pasha, J. Theerthagiri, S. Manickam, M. Y. Choi, *Coord. Chem. Rev.* **2022**, 462, 214518.
- [21] L. Lin, J. Chen, D. Liu, X. Li, G. G. Wallace, S. Zhang, *Adv. Energy Mater.* **2020**, 10, 2002621.
- [22] K. Jayaramulu, M. Horn, A. Schneemann, H. Saini, A. Bakandritsos, V. Ranc, M. Petr, V. Stavila, C. Narayana, B. Scheibe, Š. Kment, M. Otyepka, N. Motta, D. Dubal, R. Zbořil, R. A. Fischer, *Adv. Mater.* **2021**, 33, 2004560.
- [23] X. Yang, Q. Wang, K. Zhu, K. Ye, G. L. Wang, D. X. Cao, J. Yan, *Adv. Funct. Mater.* **2021**, 31, 2101087.
- [24] T. Guo, M. Fu, D. Zhou, L. Pang, J. Su, H. Lin, X. Yao, A. S. B. Sombra, *Small Struct.* **2021**, 2, 2100015.
- [25] C. Zhang, V. Nicolosi, *Energy Storage Mater.* **2019**, 16, 102.
- [26] Z. Sun, S. Fang, Y. H. Hu, *Chem. Rev.* **2020**, 120, 10336.
- [27] L. Cao, C. Wang, Y. Huang, *Chem. Eng. J.* **2023**, 454, 140094.
- [28] L. Niu, Q. Yang, W. Wang, Y. Yang, J. Xu, Q. Li, *J. Energy Storage* **2023**, 58, 106453.
- [29] S. P. Lee, G. A. M. Ali, M. A. Assiri, K. V. Kong, E. Y. L. Teo, K. F. Chong, *Appl. Surf. Sci.* **2023**, 613, 156069.
- [30] O. B. Abdillah, O. Floweri, M. A. Irham, A. H. Aimon, T. Ogi, F. Iskandar, *Energy Fuels* **2022**, 36, 14453.
- [31] X. Yu, N. Li, S. Zhang, C. Liu, L. Chen, M. Xi, Y. Song, S. Ali, O. Iqbal, M. Han, C. Jiang, Z. Wang, *J. Mater. Chem. A* **2022**, 10, 3382.
- [32] L. Wang, H. Yao, F. Chi, J. Yan, H. Cheng, Y. Li, L. Jiang, L. Qu, *ACS Nano* **2022**, 16, 12813.
- [33] T. Pinheiro, R. Correia, M. Morais, J. Coelho, E. Fortunato, M. G. F. Sales, A. C. Marques, R. Martins, *ACS Nano* **2022**, 16, 20633.
- [34] Z. Li, J. Lin, B. Li, C. Yu, H. Wang, Q. Li, *J. Energy Storage* **2021**, 44, 103437.
- [35] V. D. Nithya, *J. Energy Storage* **2021**, 44, 103380.
- [36] J. Zeng, C. Xu, T. Gao, X. Jiang, X. Wang, *Carbon Energy* **2021**, 3, 193.
- [37] H. Cheng, Q. Li, L. Zhu, S. Chen, *Small Methods* **2021**, 5, 2100502.
- [38] M. Rapisarda, F. Marken, M. Meo, *Commun. Chem.* **2021**, 4, 169.
- [39] A. Velasco, Y. K. Ryu, A. Boscá, A. Ladrón-de-Guevara, E. Hunt, J. Zuo, J. Pedrós, F. Calle, J. Martinez, *Sustainable Energy Fuels* **2021**, 5, 1235.
- [40] A. Huang, M. F. El-Kady, X. Chang, M. Anderson, C.-W. Lin, C. L. Turner, R. B. Kaner, *Adv. Energy Mater.* **2021**, 11, 2100768.
- [41] N. An, Z. Guo, J. Xin, Y. he, K. Xie, D. Sun, X. Dong, Z. Hu, *J. Mater. Chem. A* **2021**, 9, 16824.
- [42] X. Chang, M. F. El-Kady, A. Huang, C.-W. Lin, S. Aguilar, M. Anderson, J. Z. J. Zhu, R. B. Kaner, *Adv. Funct. Mater.* **2021**, 31, 2102397.
- [43] Y. Gogotsi, R. M. Penner, *ACS Nano* **2018**, 12, 2081.
- [44] Y. Peng, M. Yu, L. Zhao, H. Zeng, T. He, M. K. Hadi, R. Liu, G. Cao, H. Dang, Y. Wu, F. Ran, *Appl. Surf. Sci.* **2023**, 612, 155903.
- [45] M. R. Biradar, C. R. K. Rao, S. V. Bhosale, S. V. Bhosale, *J. Energy Storage* **2023**, 58, 106399.
- [46] M. Xu, X. Wang, Z. Li, X. Tan, M. Yang, J. Zhao, *J. Alloys Compd.* **2023**, 938, 168568.
- [47] C. Jiang, M. Gao, S. Zhang, L. Huang, S. Yu, Z. Song, Q. Wu, *Int. J. Biol. Macromolecules* **2023**, 225, 1437.
- [48] R. Joshi, A. D. Adhikari, A. Dey, I. Lahiri, *Mater. Sci. Eng., B* **2023**, 287, 116128.
- [49] M. Maghshenas, M. Mazloum-Ardakani, L. Amiri-Zirtol, F. Sabaghian, *Int. J. Hydrogen Energy* **2021**, 46, 30219.
- [50] T. N. J. I. Edison, R. Atchudan, N. Karthik, P. Chandrasekaran, S. Perumal, P. Arunachalam, P. B. Raja, M. G. Sethuraman, Y. R. Lee, *Surf. Coat. Technol.* **2021**, 416, 127150.
- [51] T. Lim, J. W. Suk, *Funct. Compos. Struct.* **2021**, 3, 015005.
- [52] S. Korkmaz, İ. A. Kariper, *J. Energy Storage* **2020**, 27, 101038.
- [53] L. Chang, Y. H. Hu, *Matter* **2019**, 1, 596.
- [54] P. Forouzandeh, P. Ganguly, R. Dahiya, S. C. Pillai, *J. Power Sources* **2022**, 519, 230744.
- [55] S. Gadipelli, Y. Lu, N. T. Skipper, T. Yildirim, Z. Guo, *J. Mater. Chem. A* **2017**, 5, 17833.
- [56] Y. Xu, Z. Lin, X. Zhong, X. Huang, N. O. Weiss, Y. Huang, X. Duan, *Nat. Commun.* **2014**, 5, 4554.
- [57] L. Zhong, C. Wu, S. Lei, G. Liang, S. Sayyar, B. Gao, L. Lin, *ACS Appl. Energy Mater.* **2022**, 5, 8004.
- [58] F. Yue, G. Gao, F. Li, Y. Zheng, S. Hou, *Carbon* **2018**, 134, 112.
- [59] G. Lee, C. Lee, C. M. Yoon, M. Kim, J. Jang, *ACS Appl. Mater. Interfaces* **2017**, 9, 5222.
- [60] Y. H. Hwang, S. M. Lee, Y. J. Kim, Y. H. Kahng, K. Lee, *Carbon* **2016**, 100, 7.
- [61] H. Huang, C. Lei, G. Luo, G. Li, X. Liang, S. Tang, Y. Du, *Carbon* **2016**, 107, 917.
- [62] Y. Peng, Y. Liu, J. Chang, C. Wu, M. Ger, N. Pu, C. Chang, *Carbon* **2015**, 81, 347.
- [63] Y. Zou, I. A. Kinloch, R. A. W. Dryfe, *J. Mater. Chem. A* **2014**, 2, 19495.
- [64] D. Li, C. Yu, M. Wang, Y. Zhang, C. Pan, *RSC Adv.* **2014**, 4, 55394.
- [65] M. F. El-Kady, V. Strong, S. Dubin, R. B. Kaner, *Science* **2012**, 335, 1326.
- [66] J. Yan, J. Liu, Z. Fan, T. Wei, L. Zhang, *Carbon* **2012**, 50, 2179.
- [67] B. Zhao, P. Liu, Y. Jiang, D. Pan, H. Tao, J. Song, T. Fang, W. Xu, *J. Power Sources* **2012**, 198, 423.
- [68] B. Lobato, L. Suárez, L. Guardia, T. A. Centeno, *Carbon* **2017**, 122, 434.
- [69] X. Yang, D. Yang, G. Zhang, H. Zuo, *J. Power Sources* **2021**, 482, 229135.
- [70] J. Castro-Gutiérrez, R. L. S. Canevesi, M. Emo, M. T. Izquierdo, A. Celzard, V. Fierro, *Renewable Sustainable Energy Rev.* **2022**, 167, 112716.
- [71] Y. Zhu, S. Murali, M. D. Stoller, K. J. Ganesh, W. Cai, P. J. Ferreira, A. Pirkle, R. M. Wallace, K. A. Cychosz, M. Thommes, D. Su, E. A. Stach, R. S. Ruoff, *Science* **2011**, 332, 1537.
- [72] S. Zhu, M. Gruschwitz, V. Tsikourkitoudi, D. Fischer, F. Simon, C. Tegenkamp, M. Sommer, S. Choudhury, *ACS Appl. Mater. Interfaces* **2022**, 14, 44772.
- [73] J. Yang, J. Meng, L. Zhang, K. Chu, W. Zong, L. Ge, S. Fu, J. Ge, H. Zhu, G. He, D. J. L. Brett, F. Lai, T. Liu, *J. Power Sources* **2022**, 549, 232111.
- [74] H. Shi, *Electrochim. Acta* **1996**, 41, 1633.
- [75] H. Ji, X. Zhao, Z. Qiao, J. Jung, Y. Zhu, Y. Lu, L. L. Zhang, A. H. MacDonald, R. S. Ruoff, *Nat. Commun.* **2014**, 5, 3317.